AIAA JOURNAL
Vol. 40, No. 4, April 2002

Experimental and Computational Investigation of Supersonic Impinging Jets

F. S. Alvi*
Florida A&M University and Florida State University, Tallahassee, Florida 32310
and
J. A. Ladd† and W. W. Bower‡
The Boeing Company, St. Louis, Missouri 63166

The results of an experimental and computational study of a moderately underexpanded axisymmetric supersonic jet issuing from a converging nozzle and impinging on a ground plane are presented. The goal of this work is to develop a better understanding of the impinging jet flowfield, which is of significant practical interest because of its presence in short takeoff and vertical landing (STOVL) aircraft during hover as well as in other aerospace-related and industrial applications. The experimental measurements include flow visualization, surface-pressure distributions, and velocity field data obtained using particle image velocimetry (PIV). The experimental data, especially the velocity field measurements, were used to verify the accuracy of computational predictions. Computational results obtained using two different turbulence models produced almost identical results. Comparisons with experimental results reveal that both models capture the significant features of this complex flow and were in remarkably good agreement with the experimental data for the primary test case. The experiments and computations both revealed the presence of the impingement zone stagnation bubble, which contains low velocity recirculating flow. Other features, including the complex shock structure and the high-speed radial wall jet, were also found to be very similar. The ability to measure and predict accurately the impinging jet behavior, especially near the ground plane, is critical because these are regions with very high mean shear, thermal loads, and unsteady pressure forces, which contribute directly to the problem of ground erosion in STOVL applications.

Introduction

HIGH-SPEED impinging jets can occur in a variety of aerospace-related applications. These jet flows are particularly troublesome to short takeoff and vertical landing (STOVL) aircraft, such the Harrier/AV-8 family, during hover mode. In these instances the flowfield produced by the impingement of the high-speed lift jets produces adverse local flow conditions, which can potentially lead to the degradation of aircraft performance in a number of areas during hover. These adverse effects, collectively referred to as ground effects, are the result of the highly unsteady nature of the flow generated by the impingement of the high-speed jet(s) on the ground plane and the pressure field caused by the natural entrainment by these jets. They include lift loss caused by flow entrainment associated with the lifting jets, which induces low surface pressures on the airframe resulting in a "suckdown" force opposite to lift. The lift loss typically increases in magnitude as the aircraft approaches the ground and can be greater than 60% of the total lift jet thrust when the jets are very close to the ground plane.[1] Increased noise or overall sound-pressure levels associated with high-speed impinging jets and the sonic fatigue of structural elements in the vicinity of the nozzle exhaust caused by unsteady loading is also an area of concern. In addition to higher levels, the noise spectrum is dominated by discrete tones, which, if close to the aircraft panel frequencies, can further aggravate the sonic fatigue problem. Furthermore, the impingement of hot, high-speed lift jets on the landing surface can lead to significant erosion caused by the extremely high shear stresses and wall heat-transfer rates created in this flow. Finally, the outwash from the hot impinging jets can be drawn into the engine inlets, a phenomenon known as hot gas ingestion, thus degrading engine performance and potentially risking engine failure.

Some of the problems just outlined are known to occur for the subsonic Harrier family of aircraft. They are expected to become more acute for the future generation of the supersonic STOVL aircraft, where the environment is expected to be more severe because of the impingement of supersonic jets operating at higher temperatures. Consequently, the study of supersonic impinging jet flows is of great interest from a practical perspective. Furthermore, the complex nature of the impinging jet flowfield, which often includes multiple shock and shock/shear layer interactions, subsonic, supersonic and separated flows, makes this flow interesting from a fundamental fluid dynamics standpoint.

Impinging jet flows have been the focus of research for over three decades, where their fluid dynamic and acoustic properties have been carefully examined by a number of capable investigators. Notable among the acoustic studies are those by Neuwerth,[2] Powell,[3] Tam and Ahuja,[4] Henderson and Powell,[5] and most recently Krothapalli et al.[1] One of the primary outcomes of these aeroacoustic studies is that the highly unsteady, oscillatory nature of impinging jet, which is accompanied by discrete, high-amplitude acoustic tones, referred to as impingement tones, is caused by a feedback loop. The globally oscillatory behavior of the jet and the resulting impingement tones have been explained well by a feedback mechanism derived from earlier work by Powell.[6] Recently, Krothapalli et al.[1] demonstrated that the feedback phenomenon might also be responsible for the lift loss, described earlier, through the generation of large-scale structures in the jet shear layer. Because the focus of the present work is the mean behavior of the impinging jet, a more detailed discussion of the unsteady properties is outside the scope of this article. The interested reader is directed to the references just cited. Suffice it to say that the fluid dynamic and acoustic properties of this flow appear to be intimately related.

The structure and fluid dynamic properties of this flow have also been investigated in a number of studies. In a classic study Donaldson and Snedeker[7,8] examined the flowfield using schlieren

Presented as Paper 2000-2224 at Fluids 2000, Denver, CO, 19–22 June 2000; received 7 August 2000; revision received 24 July 2001; accepted for publication 20 September 2001.

*Associate Professor, Fluid Mechanics Research Laboratory, Department of Mechanical Engineering. Senior Member AIAA.
†Engineer/Scientist, Mailcode 1067126, P.O. Box 516. Member AIAA.
‡Boeing Technical Fellow, Mailcode 1067126, P.O. Box 516. Associate Fellow AIAA.

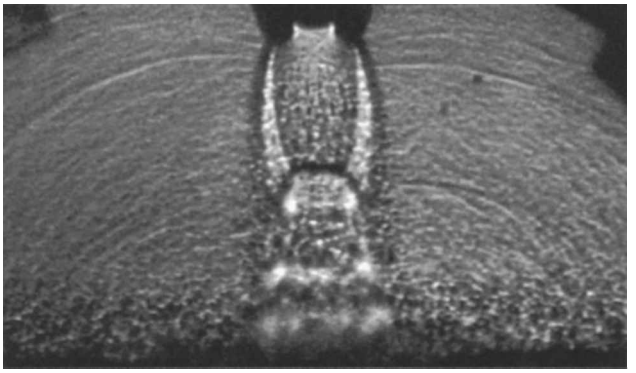

a) Shadowgraph

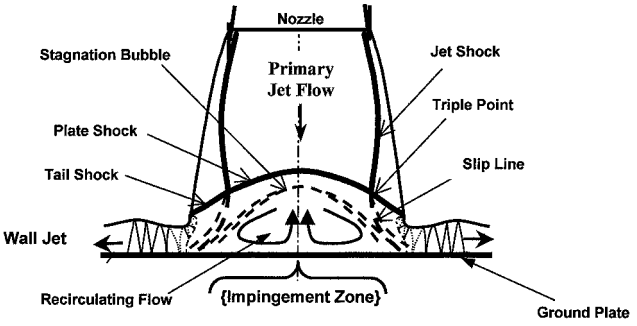

b) Flowfield schematic

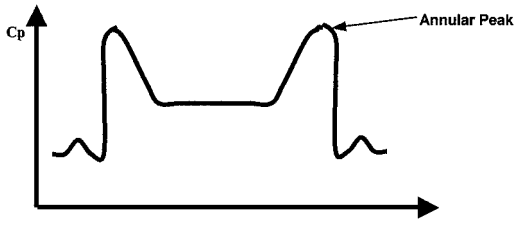

c) Pressure distribution

Fig. 1 Stagnation bubble flowfield.

photography, surface flow visualization, mean surface-pressure measurements, and, to a limited extent, surface heat-transfer rates. Carling and Hunt[9] and Lamont and Hunt[10] have further studied this flow, concentrating on the impingement zone, which lies at the center of the flowfield, and the wall jet region (see Fig. 1). In addition, Gubanova et al.,[11] Ginzberg et al.,[12] and Gummer and Hunt[13] have also examined the flow structure in detail, particularly in the impingement zone. The impingement zone is perhaps the most important and certainly the most complex part of this flow, and although previous studies have provided some insight into this flow region some issues such as the conditions for the formation of a stagnation bubble in the impingement zone[11,13] are still not well understood. Further discussion of this issue is delayed until the beginning of the Results and Discussion section; a more detailed review of this issue can be found in Alvi and Iyer.[14] In summary, although earlier studies provided valuable insight into the flowfield behavior, they mainly relied on measurements of mean surface-pressure distributions and surface flow visualization. Until recently, very little quantitative data have been available in the flowfield above the surface, especially in the critical near-surface flow in the impingement and wall-jet regions.

To address some of these issues and to gain a better understanding of supersonic impinging jet flows, especially their behavior in the context of STOVL aircraft, a comprehensive experimental investigation of the impinging jet flowfield was initiated at the Fluid Mechanics Research Laboratory (FMRL), Florida A&M University and Florida State University, Tallahassee, Florida, a few years ago. One of the most notable contributions of this ongoing experimental effort has been the velocity field data obtained using the particle image velocimetry (PIV) technique. To the authors' knowledge these data are the first of their kind to provide detailed velocity and vorticity field information over the entire flow. The PIV measurements combined with acoustic data, flow visualization, and mean and unsteady pressure fields have provided significant insight into the overall behavior of this flow. In addition to the experimental study, a collaborative computational effort was also initiated with The Boeing Company. Boeing is performing computational fluid dynamics (CFD) for selected test cases where the experimental data have been used to benchmark the computational code in order to establish its accuracy. Previous studies of free and impinging compressible jets have been made at Boeing by Wlezien et al.,[15] who computed acoustic fields from a direct Navier–Stokes simulation and the acoustic analogy equation. An assessment of several one- and two-equation turbulence models for twin impinging jets was made by Ladd and Korakianitis,[16] who obtained good predictions of impingement region velocity data and fair predictions of upwash fountain properties when compared to water-tunnel laser doppler velocimetry data. Detailed results of some of these experimental studies addressing the aeroacoustic properties of the single impinging jet flows have been published by Krothapalli et al.[1] and Alvi and Iyer.[14] In the present paper we present a review and comparison of significant experimental and computational results for selected relevant cases. By combining experimental and computational results, one might gain further insight into physics governing this complex flow, thus revealing the value of such collaborative computational and experimental studies. A discussion of the strengths and weaknesses of the computational code and suggestions for future improvement is also presented.

Experimental Methods

Test Models and Facilities

The relatively simple configuration used for the experimental and computational study is shown in Fig. 2. It consists of an axisymmetric nozzle, which produces the high-speed jet impinging on a ground plane. For some cases a circular disk, referred to as a "lift" plate, is placed at the nozzle exit plane. The disk has an annular hole from which the jet issues and is meant to represent a generic outer moldline from which the jet exhausts. The relevant geometric parameters, also indicated in Fig. 2, include d, the nozzle exit diameter; D, the lift plate diameter; and h, the distance between the ground plane and the nozzle exit. Two axisymmetric nozzles, a Mach 1.5 C-D and a converging or sonic nozzle both with identical throat diameters of 25.4 mm, are used to generate the primary flow. The diameter of the lift plate is approximately $10d$ or 25.4 cm. The experimental studies were conducted using both nozzles over a wide range of nozzle pressures and ground plane distances, with and without the lift plate[1,14]; however, in the present paper discussion will be limited to the sonic nozzle operating at a fixed pressure ratio without the lift plate. The test conditions for the primary case used for comparison in this study are as follows: nozzle pressure ratio (NPR) = 5, where NPR is defined as the ratio of the jet stagnation pressure P_0 to ambient pressure P_∞ at the nozzle exit. The ambient pressure was assumed to be constant at 14.7 psia, hence the jet was operated at $P_0 = 73.5 \pm 0.5$ psia. The nominal jet stagnation temperature for the experimental study was 20°C. The ground plane was a distance of three diameters from the nozzle exit ($h/d = 3$) for the primary test case; results for other ground plane heights are also briefly discussed to examine the influence of nozzle height on the flow behavior.

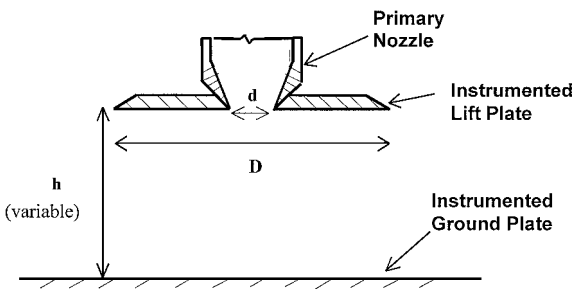

Fig. 2 Supersonic impinging jet test configuration.

The experiments were conducted in the STOVL facility of FMRL. A high-pressure blowdown compressed air facility was used to supply air to the nozzles. The air is stored in a bank of large-capacity storage tanks, which are supplied by a high-displacement reciprocating air compressor. To simulate different aircraft heights above the ground, the ground plane is mounted on a hydraulic lift and can be moved relative to the model. In the experiments described here, the ground plane consisted of an instrumented 1×1 m aluminum plate, which was centered underneath the model. More details of the STOVL hover rig can be found in Wardwell et al.[17]

Measurement Techniques

To obtain whole-field velocity data in this flow using PIV, the primary jet was seeded with small (~ 1 μm) oil droplets generated using a modified Laskin nozzle, and the ambient air was seeded with smoke particles approximately 5 μm in diameter using a Rosco fog generator. The flow was illuminated with a thin light sheet generated by a dual-head Spectra Physics Nd-Yag laser with a repetition rate of 15 Hz. Each PIV image pair was acquired using a Kodak ES1.0 digital video camera capable of recording 8-bit digital image pairs in separate frames at a rate of 15 image pairs/s. Further details of this PIV technique can be found in Refs. 1 and 14. One of the main advantages of this PIV technique is a novel processing scheme with high spatial resolution that uses image matching to extract the particle displacements, hence the velocities, from particle image pairs.[18] This image-processing technique allows for measurements to be made in regions of high velocity gradients.

Despite the use of the advanced processing scheme, particle lag is inherent in any particle-tracking scheme, and some lag will always occur. This is especially true in regions with very high velocity gradients, such as in the vicinity of shock waves. Consequently, it is expected that the location of strong shocks will be partially "smeared" because of particle lag. Similarly, although to a lesser extent, particle lag will also occur in other regions with high velocity gradients such as the wall jet or in the large-scale vortical structures with highly rotational flow. In addition, in areas very close to the surface, such as the impingement zone and the wall jet, reflections of the laser sheet by the surface can also lead to larger errors in the velocity field and/or yield regions where velocity data cannot be obtained. Ross et al.[19] conducted a detailed investigation of the effect of particle size and shock strength on the accuracy of PIV measurements using an earlier and less accurate processing scheme. Their measurements show that for ~ 1 μm seed particles, particle deceleration caused by a strong oblique shock begins within 1 mm of the actual shock location, where the deceleration rate increases with increasing shock strength. Hence, we expect that the initial location of the normal shock, the strongest possible shock, should be accurately represented within 1–2 mm in the PIV data. A more detailed investigation of the particle lag is outside the scope of this paper, and the reader is referred to Ross et al.[19] and Alvi and Iyer[14] for a more comprehensive discussion. The conclusions regarding the flowfield behavior that are reached in light of the PIV velocity field data will not be materially affected. This is particularly true for the present paper where the PIV data are used only to examine the mean flow features and behavior. It is impossible to determine the absolute uncertainty of the PIV measurements because detailed velocity field data are not available in literature for this flowfield—a motivation for the present study. However, in the absence of shock waves the mean velocity field data obtained using PIV show that the velocity data are in very good agreement, in general within 3%, with the exit velocity calculated using isentropic relations. The mean PIV results presented in this paper were obtained by averaging 80 image pairs. Although a larger number of images were recorded for most cases, using more than 80 image pairs did not change the mean velocity field.

The mean surface-pressure distributions were obtained by sequentially scanning a series of surface-pressure taps along a radial line on the ground plane. The pressures were scanned using a Scanivalve™ unit connected to a Validyne strain-gauge transducer. Several seconds of data were digitized and recorded at each port to obtain an accurate measurement of the mean surface pressures. The surface pressures were measured with an accuracy of ± 0.3 psia, which translates to an uncertainty in the pressure coefficient Cp (defined later) of ± 0.005. In addition to the mean pressure ports, the ground plane was also equipped with high-frequency pressure transducers to allow for unsteady surface pressures to be measured; however, the unsteady properties will not be discussed in this paper, and the reader is referred to Refs. 1 and 14. Mean and instantaneous flow visualization images were obtained using a shadowgraph system with a field of view of approximately 30 cm in diameter. The shadowgraph system employed a conventional single pass arrangement with a collimated beam; a variable frequency, white light stroboscopic flash unit was used as the light source.

Computational Methods

The computations were conducted using the WIND computer program. This flow solver is based on a time-marching solution to the Reynolds-averaged Navier–Stokes equations. The code is applicable for flow speeds ranging from approximately Mach 0.05 to hypersonic and supports a variety of flow types including finite rate, chemically frozen, and perfect gas. The full form of the stress tensor is used (no thin-layer approximations). The equations are solved via an approximately factored upwind scheme that has been shown to be second-order accurate in physical space. A more detailed description of the numerical procedure can be found in Bush[20] or Cain and Bush.[21] Ideal gas is assumed in the present work, and Sutherland's law is used to vary the laminar viscosity as a function of temperature. The molecular and turbulent Prandtl numbers are assumed constant at values of 0.72 and 0.9, respectively. To minimize computation times, all solutions presented in this paper were obtained assuming axisymmetric flow.

In the WIND program flow turbulence can be represented using algebraic, one-equation, or two-equation modeling. For the present study three different types of turbulence models were employed. These included the one-equation Spalart–Allmaras model,[22] the two-equation shear stress transport (SST) model,[23] and the Spalart–Allmaras model with a correction for streamline curvature and system rotation (SARC).[24] As the results will show, both the two-equation SST model and the one-equation SARC model provide very similar results, which are both in very good agreement with the experimental data.

Spalart One-Equation Model with Rotation and Curvature Correction

Various corrections have been introduced in the past by other researchers, such as Launder et al.[25] and Park and Chung,[26] to account for streamline curvature and rotation. These corrections, however, are applicable only to the specific flows for which they were designed. To account for these phenomena for general flow applications, more complex turbulence models such as Reynolds-stress formulation have been employed. These sophisticated models require fewer assumptions than one- or two-equation models but are too computationally intensive to be practical for routine engineering applications. Recently, the curvature correction modification of Spalart and Shur[24] has been added to the baseline Spalart model and applied to several three-dimensional configurations.[27] The baseline Spalart model has been shown to produce results similar to the two-equation SST model for many flows but does not perform as well for problems such as the supersonic impinging jet where the shear-layer growth rates and strong rotation effects are significant. Differences between predictions from the baseline Spalart and SARC one-equation models are presented for some cases in this paper and are studied more in depth in Mani et al.[27]

Shear-Stress Transport Two-Equation Model

The SST two-equation turbulence model from Menter[23] is now used routinely in many aerospace CFD applications at The Boeing Company, St. Louis, Missouri. It is a blended model that exploits the advantages of both the k–ε model and the k–ω of Wilcox.[28] The k–ε models, such as those from Jones and Launder,[29] have numerical difficulties when attempting to integrate to the wall. There are assumptions about the boundary values of ε, which give rise to a high degree of numerical stiffness in this region. Conversely, the k–ε model does quite well for free shear-layer problems, particularly in two dimensions. The main advantage of the k–ω model is

that it behaves well for wall-bounded problems because of the physically sound boundary conditions on both k and ω. The Menter SST model employs the Wilcox k–ω model near the wall but transitions to the k–ε model via a switching function. This model is sometimes referred to as the SST model because it has the ability to account for the transport of the principal turbulent shear stress in adverse pressure gradient boundary layers. This modeling feature is based on Bradshaw's[30] assumption that the principal shear stress is proportional to the turbulent kinetic energy and is expressed through a modification of the eddy viscosity. The interested reader is referred to the original paper by Menter[23] for details of this two-equation turbulence model formulation.

Results and Discussion

Before a detailed discussion and comparison of the experimental and computational results, we provide an overview of the global impinging jet flowfield noting some of its principal features. Figure 1a shows an instantaneous shadowgraph of the principal test case, NPR = 5, $h/d = 3$; shown directly below the shadowgraph image is a schematic of the impinging jet flowfield model (Fig. 1b) and a corresponding pressure distribution sketch (Fig. 1c). The impinging jet flowfield can be divided into three main regions.[7] The first region is the main jet column, where the flow is primarily inviscid and contains expansion and compression/shock waves for nonideally expanded jets. The impingement zone is the second region and is an area in the vicinity of the jet impingement point characterized by strong gradients leading to significant changes in local flow properties. This area is also referred to as the shock layer. Finally, the radial wall jet, the third distinct region, is the area outside the impingement zone, which contains the jet flow redirected radially outward after impingement. All three zones have been indicated in Fig. 1b. The flow schematic depicts the impingement region with a stagnation bubble, and the sketch of the surface-pressure distribution beneath shows the distinctive pressure profile corresponding to the presence of a stagnation bubble. Surface-pressure distributions with such annular peaks are commonly used as distinct indicators of the presence of a stagnation or separation bubble; for cases where a stagnation bubble is not formed, the surface-pressure distribution shows a central peak. The details of the impinging jet flow features (e.g., shape of the plate and tail shocks) are strongly dependent on the jet Mach number and the ground plane distance and will vary from the sketch in Fig. 1b.

The presence, and the reasons for the formation, of a stagnation bubble have been and remain the subject of some debate. Gubanova et al.,[11] Gummer and Hunt,[13] and Kalghatgi and Hunt[31] have conducted detailed investigations of the impinging jet flow structure, particularly in the impingement zone, for a range of conditions. These investigators discuss reasons for the formation (or lack thereof) of a stagnation bubble. The interested reader is referred to these references, especially the study by Kalghatgi and Hunt,[31] which specifically addresses this issue. Very briefly, as the supersonic flow in the primary jet approaches the ground plane, it decelerates through the formation of a plate shock. If the jet is not ideally expanded, oblique shocks in the jet plume (indicated as "jet shocks" in Fig. 1b) interact with the plate shock resulting in the well-known triple-shock structure, where the third shock is generally referred to as the tail shock. It is the nature of this interaction that appears to determine the flowfield in the impingement zone. When present, the stagnation bubble was hypothesized to enclose a region of recirculating fluid with relatively low velocities. However, until the present study very little direct and detailed evidence of the flow in this stagnation bubble has been available, and the nature of the flow in the stagnation bubble had primarily been understood through interpretation of surface-pressure distributions, surface streakline patterns,[7,9] and schlieren or shadowgraph flow visualization.

Experimental Velocity Field

As already mentioned, detailed, whole flowfield velocity measurements were obtained using PIV for a range of NPRs and ground plate distances using both sonic and converging–diverging nozzles, with and without the lift plate. However, in this paper the discussion will be limited to the sonic nozzle without the lift plate, operating at NPR = 5 with the ground plane at $h/d = 3$. This was selected as our feature case because, as the shadowgraph image and the flowfield sketch in Fig. 1 reveal, the flow is very complex with shock/shock and shock/shear-layer interactions and areas of flow acceleration and deceleration into locally supersonic and subsonic regions. All PIV measurements are obtained in the central plane of the jet. The mean velocity field for the primary test case is shown in Fig. 3, where the vector plot has been overlaid on the out-of-plane vorticity color contour plot on the left half of the figure. The right half displays the streamline pattern superposed on the vorticity contours, where the units of vorticity for this and other similar vorticity contours are s^{-1}. In the velocity vector plots shown in this paper, the length of the vector is proportional to the velocity magnitude. The streamline patterns were created from the measured velocity vector field using the software package TecPlot™.

Several features are clearly revealed in Fig. 3. First, the shear layer at the jet boundary is readily apparent as a region of high vorticity in the vorticity contour plots. As the jet shear layer approaches the surface, it turns outward around $r/d \approx 1$ and forms the outer boundary of the wall jet. Also clearly evident in this figure is the presence of the strong Mach disk shock revealed by the dramatic decrease in the flow velocity, apparent from the change in vector lengths. The velocity field data show that the Mach disk occurs around $y/d \approx 1.8$,

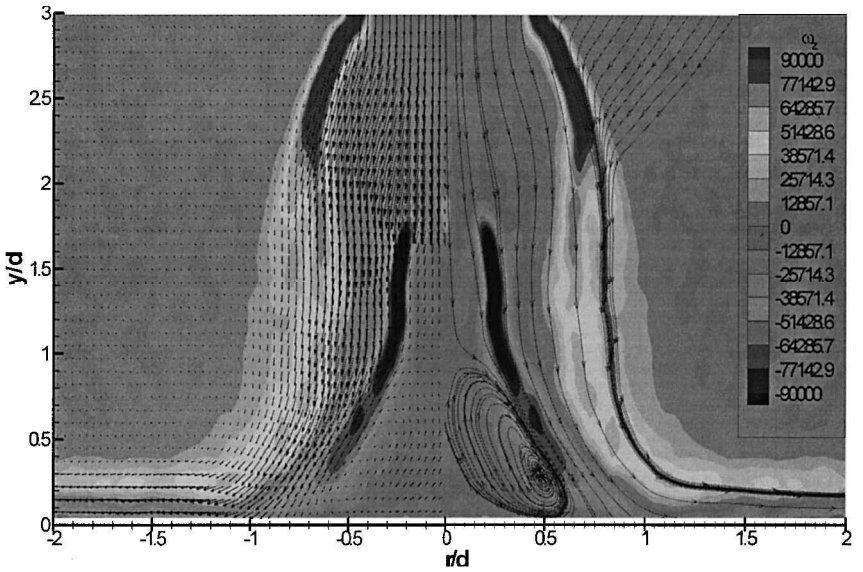

Fig. 3 Experimental vorticity contour plot with velocity vectors and streamlines: sonic nozzle, NPR = 5, $h/d = 3$.

which roughly corresponds to the Mach disk location observed in the instantaneous and mean shadowgraphs shown in Figs. 1a and 4, respectively. One of the most striking features observed in Fig. 3 is the region of recirculating flow, the stagnation bubble, in the center of the impingement zone. The presence and extent of the recirculating flow in the stagnation bubble is best revealed in the streamline plot in the right half of Fig. 3. The streamline plot also shows that the impinging flow is divided into two streams, where the outer one flows into the wall jet while the inner stream is wrapped into the stagnation bubble. In addition to the outer shear layer at the jet periphery, the inner shear layer or slip line is also visible in the vorticity plots as a region of high shear. Because the slip line emanates from the triple-shock intersection, the beginning of the inner shear layer should in principle correspond to the triple-point location on the shadowgraphs. Although the precise location of the triple point is difficult to determine from the shadowgraphs, its relative location on the PIV plots and shadowgraphs is approximately the same. The region where the inner shear layer impinges on the ground plane approximately coincides with the location of the annular pressure peak on the measured surface pressure distribution for this case (shown in Fig. 5). Although not shown here, the slip-line impingement locations in the PIV data and the annular peaks in the mean surface-pressure distributions were found to be in agreement for most of the cases examined.[14] This lends some credence to the hypothesis proposed by earlier investigators,[11] who suggested that the impingement of the slip-line flow leads to the formation of the separation bubble.

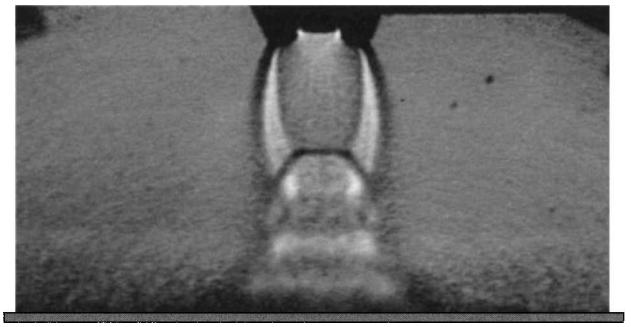

Experiment: shadowgraph

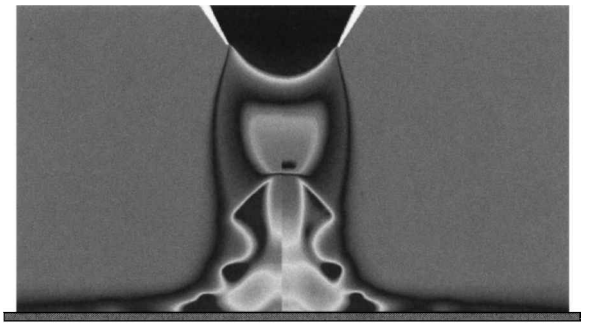

CFD computed: density contours

Fig. 4 Comparison of mean shadowgraph image and density contours from two turbulence models: sonic nozzle, NPR = 5, $h/d = 3$.

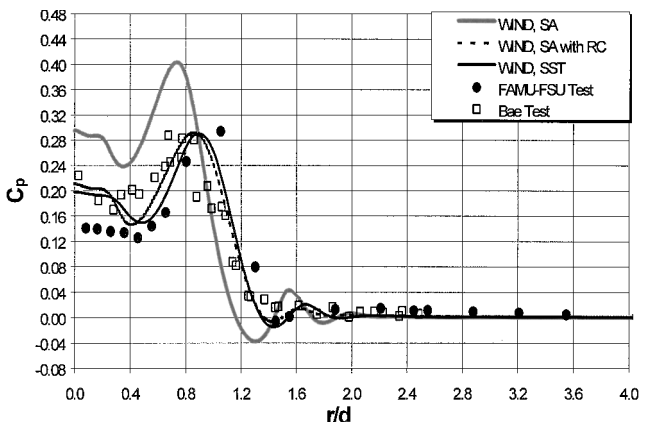

Fig. 5 Computed and measured ground plane pressures for sonic nozzle, NPR = 5, $h/d = 3$.

Comparison of Computational Results from Different Turbulence Models

Initially we will compare computational results for the primary test case using the SARC and SST turbulence models to determine the relative accuracy of each model. This will be followed by a comparison between the experimental and computational results with each of the two models. As mentioned before, the NPR = 5, $h/d = 3$ case was selected because of the complexity of the flow revealed by the measurements where a strong shock appears in the jet plume followed by a recirculation bubble near the ground plane. An axisymmetric grid plane containing five zones and nearly 30,000 points was employed for the simulation. Almost two-thirds of this number were concentrated in the nozzle plume and wall-jet formation region.

Initial attempts at using local time stepping to obtain a steady-state solution for this case yielded large oscillations in the shear-layer and wall-jet formation regions. This unsteady behavior, supported by experimental data,[14,32] then required the computation to be made using the time-accurate mode of the program. The solution from the relaxation method was then used only to provide an initial solution for the unsteady computation. In the time-accurate calculation integration of the dependent variables is obtained using a constant time interval at all spacings. This time interval must be chosen to be sufficiently small so that the numerical scheme remains stable at the smallest grid points having the largest flow gradients. This same time interval must then be used at all grid points to preserve the time accuracy. This approach, although requiring many more iterations, allows an estimate of the time-averaged flowfield to be obtained. The temporal scheme used for the current simulations is first order, but, as shown in the following sections, it still yields fairly accurate estimates of the mean flowfield. The mean flow data are obtained by averaging the data over several hundred time intervals, each interval being around 1.5 μs. These intervals are approximately five times larger than the required 0.3-μs time interval used as the integration step in the numerical scheme. Several time averages of different numbers of samples were found to produce the same mean flowfield as long as at least 50 1.5-μs intervals were averaged. This number of samples represents a good compromise between resolving the higher-frequency content of the flow and keeping the required amount of data storage to a manageable level. The computation time for a typical two-dimensional unsteady problem is then roughly 20 CPU hours on a single-processor SG-O_2 workstation.

A comparison of the computed Mach-number contours from the SARC and the two-equation SST model is shown in Fig. 6. There is a strong shock present for this configuration, which occurs after the flow expands to nearly $M = 2.8$. The shock location is seen to be approximately the same for both models. It has been determined that an accurate prediction of the location and strength of this shock is vital in obtaining a good prediction of the recirculation bubble shown in Fig. 6 and the streamline patterns in Fig. 7.

The Mach contours in Fig. 6 indicate that the computed growth of the radial wall-jet thickness is slightly higher from the SARC model. The mean streamline traces are seen to be nearly identical from both methods and are consistent with the experimental observations. The excellent agreement in the computational results using the two models is clearly evident in these and subsequent plots. Both models appear to capture the essential features of this flow; a more detailed comparison between experimental and computational results is presented in the following section. In a numerical study for a limited number of cases, Kitamura and Iwamoto[33] computed the presence of such a stagnation bubble. However, their published results were of limited resolution, and the comparison to experimental results was nominal. To the authors' knowledge, the present work provides the first detailed comparison of experimental and computational results for this flowfield, especially in the

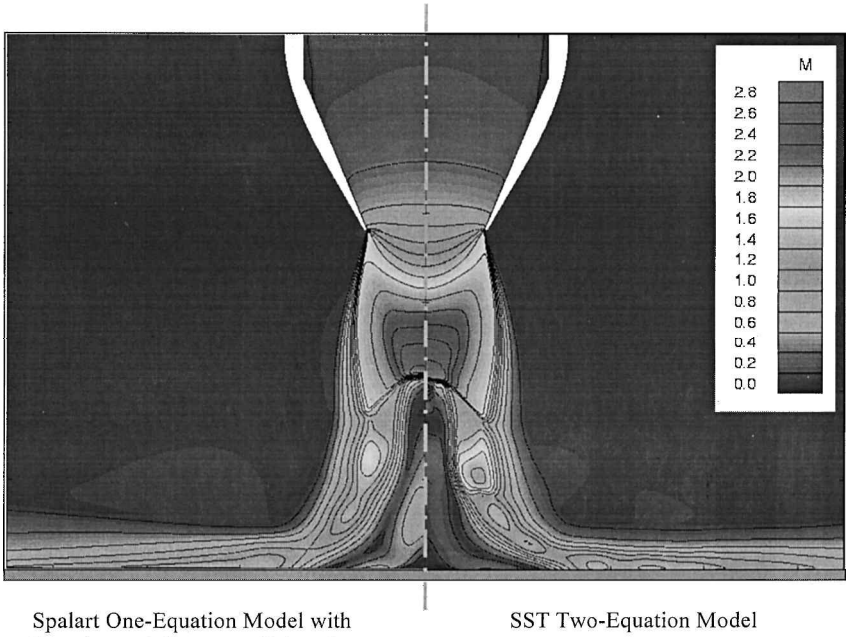

Fig. 6 Comparison of computed Mach-number contours using two turbulence models: sonic nozzle, NPR = 5, $h/d = 3$.

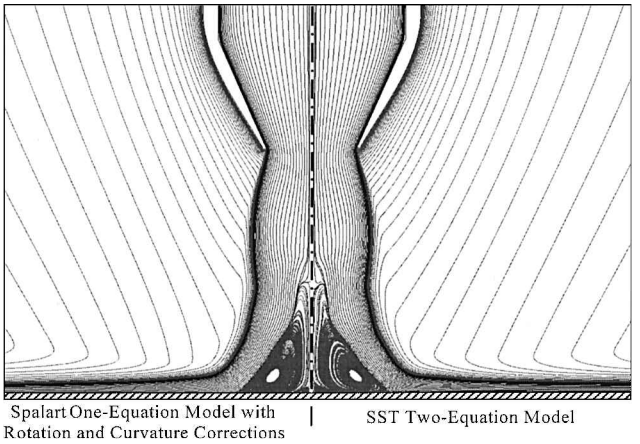

Fig. 7 Computed streamline paths using two turbulence models: sonic nozzle, NPR = 5, $h/d = 3$.

impingement and wall-jet regions, at a level of resolution not obtained before.

Although the computed data presented in the current work were obtained using the full 30,000-point computational grid, simulations using half the number of points in the vertical and lateral direction yielded nearly identical results. This is a good indication of grid independence and that adding additional points in the domain will not improve the accuracy. The mesh was constructed so that the height of the first point above the wall is near $y^+ = 3$ at the location of maximum wall-jet velocity near $r/d = 1.25$. Unfortunately, the tight clustering at this location limits the maximum stable time-step size that can be used for the entire simulation.

Comparison of Experimental and Computational Results: Primary Test Case

An example of a time-averaged shadowgraph revealing the flow structure can be seen in Fig. 4. This figure also shows mean density contours from the CFD simulation using both models. A direct comparison among the details observed in the shadowgraphs and density contours is not strictly valid because a shadowgraph is an integrated image, sensitive to the second spatial derivative of density in the flowfield. However, a comparison in the overall flow structure and primary flow features can still be made. Computed density contours from both turbulence models are almost identical, and there is a striking similarity between the computed flow structures with features observed in the shadowgraph. The triple-shock structure, which includes the jet shock, tail shock, and the Mach disk, is captured by the computations, and their locations approximately coincide with the experimental observations. The computed density contours also reveal the presence of the inner shear layer and the outer boundaries of the stagnation bubble.

To further assess the accuracy of the CFD predictions, comparisons are presented in Fig. 8 of the line contours plots of the mean velocity field obtained from the PIV data and the computation using the SST turbulence model. The computed data have been interpolated to the same locations represented by the PIV data for a direct comparison. Only the velocity contours from the SST model are presented in this figure, although results from the SARC model (not shown) are nearly identical. Once again, the computations predict the measured velocity field very well with some discrepancies. Both computational models predict the location of the Mach disk slightly closer to the ground plane than does the measurement. Consequently, the vertical extent of the separation bubble is also marginally underpredicted. The magnitude and extent of the high velocity region in the jet core, upstream of the Mach disk, is somewhat higher in the PIV measurements than in the CFD predictions, and there is a discrepancy in the velocity magnitudes in the wall jet, very close to the wall. However, it is clearly evident that overall the computations yield very good predictions for the entire flowfield, including the jet core velocities, the recirculation region, and in the wall jet. These characteristics are of critical importance from a practical perspective because of their influence on ground erosion.

The comparison between CFD and PIV results continues in Fig. 9, which shows the mean vorticity contours and the velocity vectors from experimental and computational data. (The numbers in parentheses above the contours indicate the grid size used for the interpolated data.) The similarity of the CFD and PIV data in the recirculation region and the overall flow structure can be easily seen. There appears to be a greater expansion angle at the nozzle exit in the experiment than what is predicted in the CFD results. Also, as in Fig. 8, the Mach disk appears closer to the ground in the computations than the PIV data, resulting in a smaller separation bubble above the surface. However, the radial extent of the stagnation bubble, defined by the impingement location of the inner shear layer/slip line on the surface, is in very close agreement with the experimental results within $r/d \sim 0.1$. This agreement in the radial extent of the stagnation bubble is also supported by the

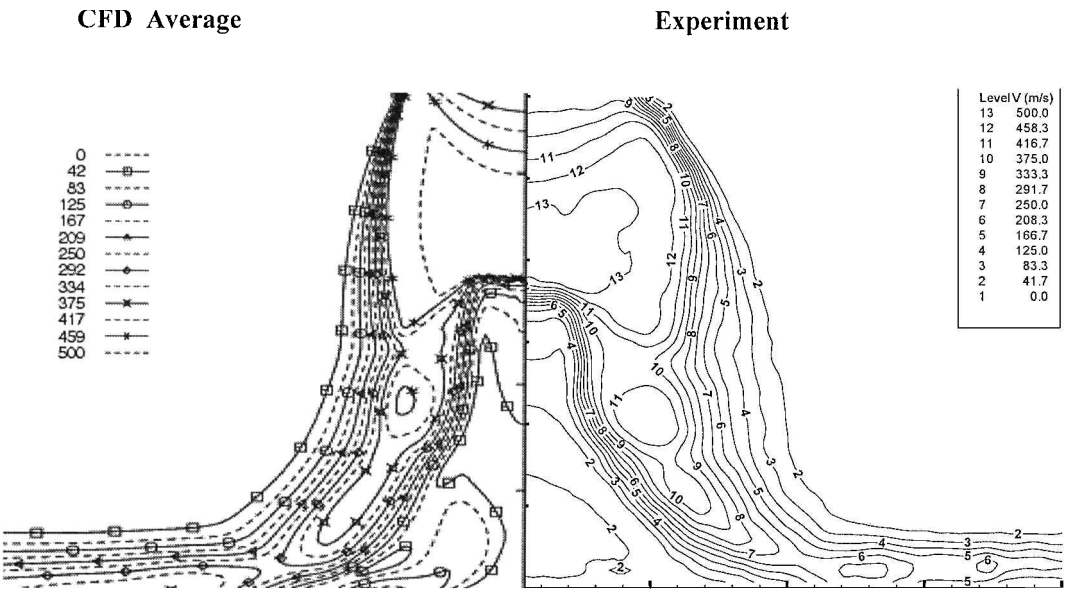

Fig. 8 Comparison of velocity contours from CFD and experimental PIV data: sonic nozzle, NPR = 5, $h/d = 3$.

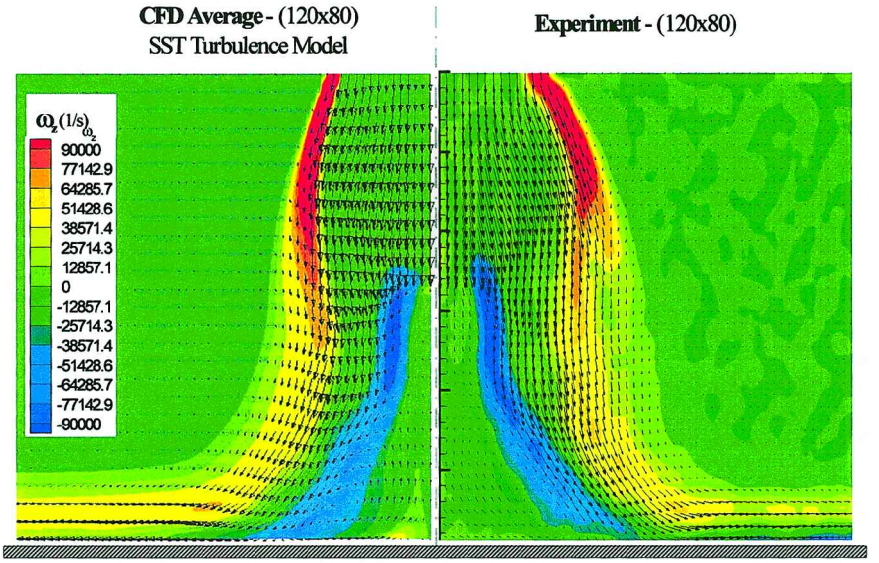

Fig. 9 Measured (PIV) and computed velocity vectors and vorticity contours: sonic nozzle, NPR = 5, $h/d = 3$.

comparison of the surface pressure distributions, presented earlier in Fig. 5. A comparison of the vorticity contours reveals the remarkable similarity in the shape and magnitude of the diffusing vorticity values between the computational and experimental results. It is clear that the vorticity field is well predicted by the computations indicating an accurate simulation of the strength and location of the primary jet shear layer, which is redirected into the wall-jet shear layer. As noted earlier, the inner shear layer that emanates from the triple point (Fig. 1b) is also extremely well predicted in terms of shape and vorticity levels.

A comparison of the predicted and measured ground plane surface-pressure distributions is shown in Fig. 5. Results from numerical solutions employing several turbulence models are included and compared to the experimental data. The dependent variable in this figure C_p represents the nondimensional surface-pressure coefficient, where $C_p = (P_s - P_\infty)/(P_0 - P_\infty)$ and P_s is the surface pressure. The x axis represents the radial location, nondimensionalized by the nozzle throat diameter, in this case same as the exit diameter d.

The overall pressure distribution with a low-pressure plateau and an annular peak is typical of an impingement flow with a recirculation bubble (Fig. 1) as discussed earlier. The pressure near the impingement point is well below the jet total pressure that is normally recovered for an ideally expanded nozzle without a separation bubble. The recirculating bubble divides the jet core and deflects it radially outward so that the peak pressure is lower than the stagnation pressure and occurs away from center of the interaction. In principle, the pressure peak should correspond to the location of the stagnation streamline in the inner shear layer, which divides the jet flow that is redirected into the wall jet from the fluid that is entrained into the recirculation bubble. This is the behavior observed in the present case where the pressure peak occurs roughly around $r/d = 1$, a location that corresponds to the impingement of the inner shear layer as seen in Fig. 9. The baseline Spalart model is seen to significantly overpredict the pressure throughout the impingement region, whereas the inclusion of the curvature formulation (SARC) produces a distribution in agreement with the SST model prediction and in much better agreement with the experimental results. A closer comparison of the SST or SARC results with the experimental data reveals that the greatest discrepancy between computational and the experimental data occurs in the central portion of the impingement zone. In this region (r/d roughly less than 0.4) both models overpredict the plateau pressure by as much as 30%. The overprediction of the pressure in this region is expected if one realizes that $r/d \leq 0.4$

roughly defines the radial extent of the Mach disk formed above the impingement zone (see Fig. 3). As noted earlier, the computations underpredict the strength of the Mach disk (see Fig. 8), which in turn would overpredict the pressures recovered downstream of the Mach disk on the impingement surface. Notwithstanding some differences in pressures in certain regions, the overall agreement between the predicted and measured distributions is very good.

In addition to the primary experimental data, surface pressures obtained for a similar configuration at British Aerospace[34] are also shown in Fig. 5. The BAe axisymmetric nozzle had an exit diameter of 120 mm and a jet total temperature of $T_t = 1800^\circ$F and operated at the same NPR as the cold jet in the present study. The plot shows that the normalized pressure distributions from this experiment are in good agreement with the present (FAMU-FSU) cold jet data and the computations. The agreement of these three data sets provides further confidence in the ability of the CFD code to capture the features of interest in this complex flowfield.

The ground erosion problem is a result of the unusually high mean and unsteady loads imparted on the impingement surface by the hot, high-speed impinging jet(s). An examination of the velocity contour plot shown in Fig. 8 illustrates that the radial wall-jet region contains fluid with very high velocities, in close proximity to the wall. As an example, Fig. 8 shows that wall-jet velocities in the range of 250–350 m/s are found within a few millimeters from the surface, resulting in very high velocity gradients and wall shear stresses. The radial distribution of the computed nondimensionalized wall shear stress, shown in Fig. 10, provides the magnitudes of the computed shear stresses for the primary test case. In this plot the ordinate depicts the skin friction C_f, defined as $C_f = \tau_w/(P_0 - P_\infty)$, where

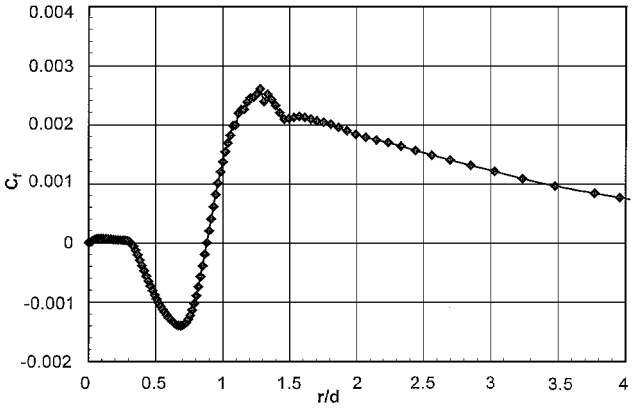

Fig. 10 Computed skin-friction distribution: sonic nozzle, NPR = 5, *h/d* = 3.

τ_w is the wall shear stress and $(P_0 - P_\infty)$ is the difference between the jet stagnation and the freestream ambient pressure.

Several points are of interest in this distribution. First, we see that the skin friction is very low, almost zero, in the central portion of the flowfield. A look at the velocity contour plot (Fig. 8) and the vorticity contour plots (Fig. 9) confirms that this area of the surface lies under the separation bubble and is a region of very low velocities and negligible vorticities, hence minimal shear stresses. Moving radially outward, there is a rapid increase in the skin friction starting at $r/d \approx 0.3$ and ending at $r/d \approx 0.7$, where a (negative) peak in the wall shear stress is present. The negative values of the shear stress are caused by the fact that fluid in the stagnation bubble is moving radially inward in this region, as illustrated in the vorticity/vector plots in Fig. 3 and Fig. 9. Figure 3 also shows that the negative peak at $r/d \approx 0.7$ roughly corresponds to the inner extent of the slip line impingement on the surface, an area where high shear stresses are expected. A more dramatic rise in the skin friction occurs between $r/d \approx 0.7$ and 1.2 with a skin friction peak at the latter location. Figure 3 clearly shows that this region corresponds to the slip-line impingement and the inception of a new boundary layer in the wall jet, which is bounded by a high-speed outer flow, hence the significantly higher shear stresses. The skin friction goes through a sign change in this area with a zero occurring at $r/d \approx 0.9$, which by definition is the location of the attachment line in the computed flow. The agreement between the zero skin-friction location and slip-line impingement point in the experimental results indicates that $r/d \approx 0.9$ is close to the actual location of the attachment line. This attachment line divides the stagnation bubble flow from the wall-jet flow, an observation supported by the surface-pressure distribution of Fig. 9, where the pressure peak occurs at the same radial location. In summary, it is clear that the jet impingement and wall-jet regions are areas of not only very high shear stresses but also large gradients in shear stresses where the flow goes through rapid changes in direction. Given the analogy between skin-friction and heat-transfer coefficients, it is reasonable to expect that this high skin friction be accompanied by high wall heating.[35] This behavior, combined with the fact that this region is dominated by very high fluctuating pressure loads,[14] can result in severe ground erosion.[34]

Comparison of Secondary Cases

Finally, we briefly compare experimental and computational results for two other cases at the same pressure, NPR = 5, and two heights, $h/d = 2$ and 1.6. Similar to Fig. 9, experimental and computational velocity vector/velocity contour plots for these two cases are shown in Figs. 11 and 12. This is followed by a comparison of the experimental and computational surface-pressure distributions for both heights shown in Fig. 13.

The comparison between CFD and PIV results for $h/d = 2$ in Fig. 11 shows an overall agreement in the computed and measured

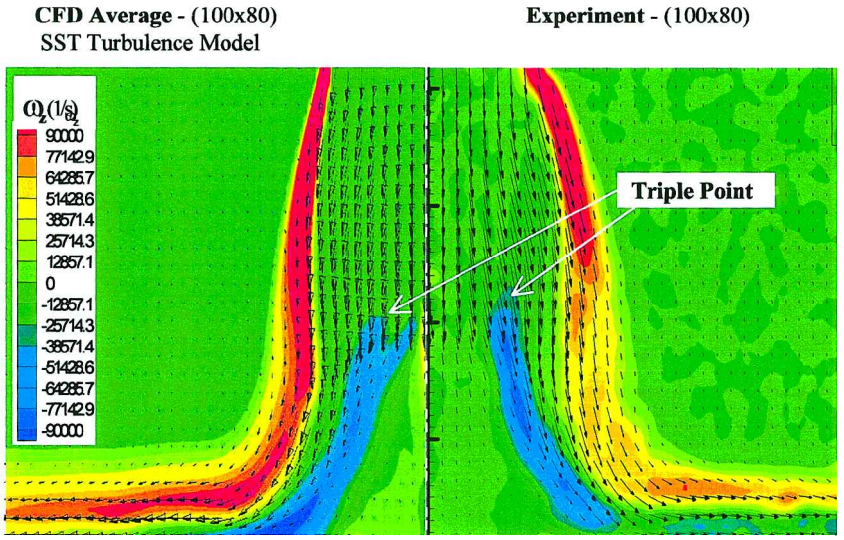

Fig. 11 Comparison of velocity vectors and vorticity contours from CFD and PIV: sonic nozzle, NPR = 5, *h/d* = 2.

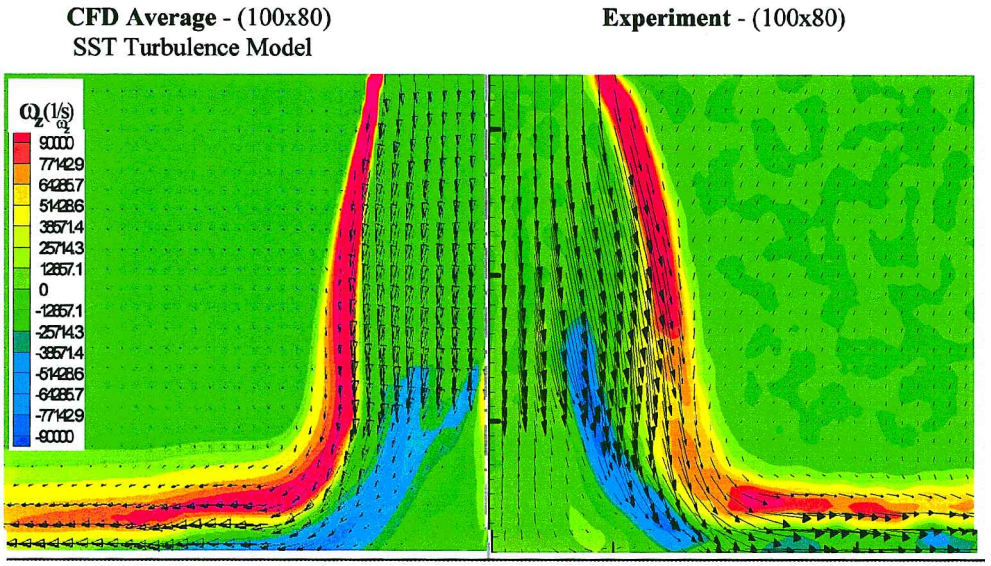

Fig. 12 Comparison of velocity vectors and vorticity contours from CFD and PIV: sonic nozzle, NPR = 5, *h/d* = 1.6.

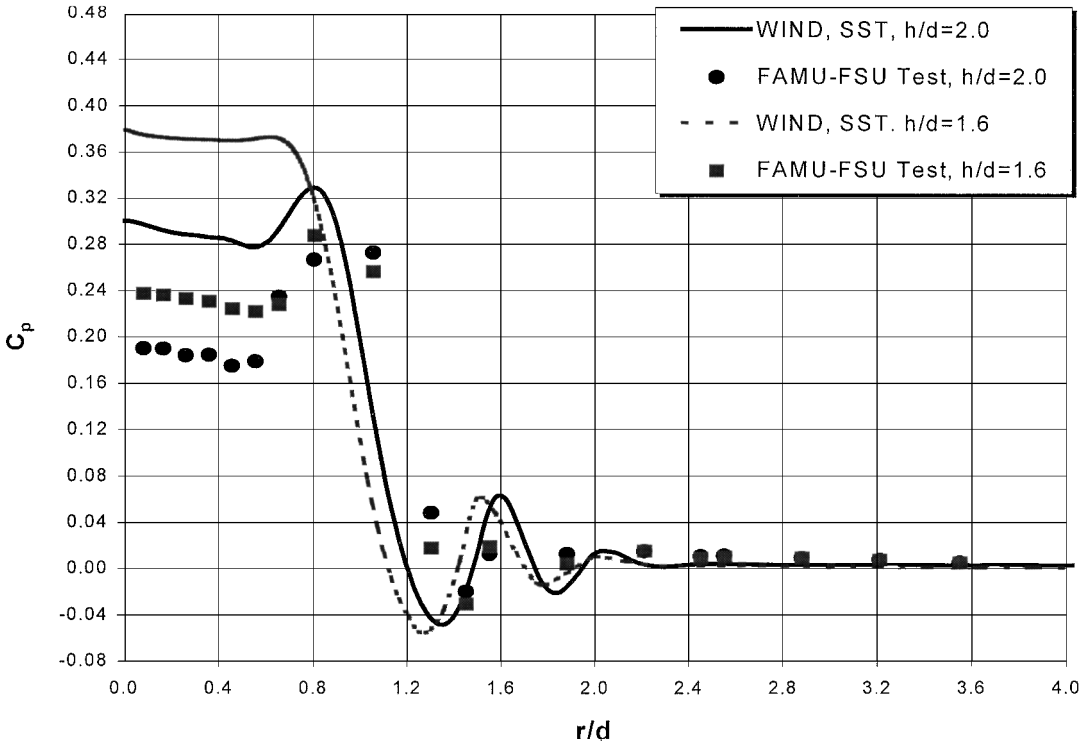

Fig. 13 Comparison of measured and computed surface-pressure distributions: sonic nozzle, NPR = 5, *h/d* = 1.6 and 2.

flow structure and the velocity field. As in the primary test case ($h/d = 3$), the Mach disk, triple point, and the inner shear layer are all captured by the computations. However, a closer look reveals that there is less diffusion of vorticity in the primary jet and wall-jet shear layer in the computed flow, where these shear layers appear more compact with higher vorticity values relative to the measured flowfield. Additionally, the triple point and the origin of the slip line (marked for clarity in Fig. 13) in the computed flowfield appears diffused, almost bifurcated, and the impingement location of the slip line is closer to the centerline than indicated by the PIV data.

As expected, these differences in the computed and measured velocity field translate into a discrepancy in the pressure distribution in Fig. 13. Although the computations reveal the presence of the stagnation bubble, indicated by the annular pressure peaks, the magnitude of the pressure in the impingement region downstream of the Mach disk is significantly overpredicted. This is presumably caused by an underprediction of the strength of the Mach disk for reasons similar to those outlined in our discussion of Figs. 5, 8, and 9 for the primary test case.

The comparison between CFD and PIV results for $h/d = 1.6$ shown in Fig. 12 follows the same trend as Fig. 11. Although overall there is good agreement between the computed and measured results, there are differences especially in the impingement region in the vicinity of the Mach disk. The triple point is much more diffused relative to the measured flow, even more so than that observed in Fig. 11. Similarly, there is a more significant difference between the experimental and computed pressure distributions (Fig. 13) in the impingement region. The computed flow for this case fails to capture the annular peak clearly present in the measured distribution.

In general, there is very good agreement between the computational results and the measured data, where the computations captured the essential features of the flow. However, it appears that, as the interaction strength increases, that is, as the nozzle to ground plane distance decreases, the differences between the two

data increase systematically. This discrepancy is generally confined to the impingement zone, a region close to the interaction centerline. It appears that the disparity might be caused by the inability of the computational scheme to accurately predict the behavior of the flow in the vicinity of the Mach disk. Differences between the experimental and computational data become more pronounced as the strength of the Mach disk increases. One reason for this behavior could be attributed to lack of adequate axial grid resolution in the region of the Mach disk. Adapting the grid distribution to the flow gradients, either manually or with true grid adaptation, would most likely increase the accuracy of the resulting numerical data. Another important consideration is the time accuracy of the numerical scheme. It is possible that the first-order scheme used in the current work suppresses some of the unsteadiness of the jet and wall shear layers, which in general become more unsteady for lower heights. This behavior would then lead to the apparent "underdiffusion" of the time-averaged vorticity contours already discussed.

Conclusions

In this paper experimental and computational results for a moderately underexpanded supersonic jet impinging on a surface were examined and compared. The ultimate goal of this work was to develop a better understanding of the impinging jet flowfield, which is of significant practical interest because of its presence in STOVL aircraft during hover. The detailed experimental results, especially the velocity field data, were used to verify the accuracy of, and served as benchmark for, the computational methods, which can be used to predict the behavior of these flows. Computational results from the SARC one-equation and SST two-equation turbulence models were nearly identical. Both models were able to capture the significant features of this complex flow and were in remarkably good agreement with the experimental data obtained for the present test case. The SST turbulence model has proven to be robust, efficient, and produce good results for a wide variety of CFD applications in the aerospace industry. The experiments and computations both revealed the presence of the stagnation bubble, at a level of resolution not seen before, which contains low-velocity recirculating flow. The complex shock structure and the high-speed radial wall jet were found to be similar in the experimental and computational data.

Although there are some discrepancies between the experimental and computational results for some cases, which become more significant with increasing interaction strength, the overall agreement is very good. It is expected that more accurate numerical simulations could be obtained through the use of a dynamic adaptive grid technique. This technique clusters the computational grid to where flow gradients are the strongest, such as shear layers and shock and expansion waves. Better resolution of these waves and other flow gradients should lead to more accurate estimations of the mean flowfield when compared to data. Also, the computed results presented here were obtained using only a first-order temporal scheme. It is believed that higher-order methods would better capture unsteady flow features and yield a more accurate prediction of the mean flowfield for a given configuration. Finally, the turbulence model plays a significant role in the accurate prediction of the impinging jet flowfield. A large source of error, in both one- and two-equation models, is the Boussinesq approximation, which must be made to obtain closure for the system of equations. This assumption allows the Reynolds-stress tensor, which arises during the averaging of the momentum equations, to be computed as the product of an eddy viscosity and the mean strain-rate tensor. Although this approximation provides accurate predictions for many flows of interest, there are some applications in which it produces large errors in flow properties when compared with measured data. The impingement of the jet flow on the ground plane gives rise to unequal normal Reynolds stresses, which will cause the Boussinesq approximation to fail. Corrections for streamline curvature, such as that of Spalart and Shur,[24] have been shown to enhance the one-equation Spalart turbulence model to yield results equal in accuracy to the more sophisticated two-equation SST model. Without the corrections the baseline Spalart model results significantly differed from the PIV velocity data including the strength and location of the Mach disk. The two-equation SST model, however, still suffers from deficiencies, which cannot be addressed until computer speeds enable large scale, cost-effective solutions to the Reynolds-stress equations or direct-numerical-simulation methods to be utilized.

The ability to measure and predict accurately the impinging jet behavior, especially near the ground plane, is critical because these are regions with very high mean shear, thermal loads, and unsteady pressure forces. An understanding of these flow characteristics is essential because they contribute directly to the study of ground erosion. We believe that this collaborative experimental and computational effort has been very fruitful and has provided unique data and insight into this complex flow behavior.

Acknowledgments

We gratefully acknowledge the continued support of NASA Ames Research Center and NASA Headquarters for sponsoring the experimental portion for this work. We appreciate the advice and help of A. Krothapalli and L. Lourenco during this study. The assistance of R. Elavarasan and K. Iyer in conducting some of the tests is also appreciated. Finally, we thank Charney Davy for her help in processing some of the data.

References

[1]Krothapalli, A., Rajakuperan, E., Alvi, F. S., and Lourenco, L., "Flow Field and Noise Characteristics of a Supersonic Impinging Jet," *Journal of Fluid Mechanics*, Vol. 392, Aug. 1999, pp. 155–181.

[2]Neuwerth, G., "Acoustic Feedback of a Subsonic and Supersonic Free Jet Which Impinges on an Obstacle," NASA TT F-15719, July 1974.

[3]Powell, A., "The Sound-Producing Oscillations of Round Underexpanded Jets Impinging on Normal Plates," *Journal of Acousical Society of America*, Vol. 83, No. 2, 1988, pp. 515–533.

[4]Tam, C. K. W., and Ahuja, K. K., "Theoretical Model of Discrete Tone Generation by Impinging Jets," *Journal of Fluid Mechanics*, Vol. 214, May 1990, pp. 67–87.

[5]Henderson, B., and Powell, A., "Experiments Concerning Tones Produced by an Axisymmetric Choked Jet Impinging on Flat Plates," *Journal of Sound and Vibration*, Vol. 168, No. 2, 1993, pp. 307–326.

[6]Powell, A., "On Edge Tones and Associated Phenomena," *Acoustica*, Vol. 3, 1953, pp. 233–243.

[7]Donaldson, C. DuP., and Snedeker, R. S., "A Study of Free Jet Impingement. Part 1. Mean Properties of Free and Impinging Jets," *Journal of Fluid Mechanics*, Vol. 45, Pt. 2, Jan. 1971, pp. 281–319.

[8]Donaldson, C. DuP., and Snedeker, R. S., "A Study of Free Jet Impingement. Part 2. Free Jet Turbulent Structure and Impingement Heat Transfer," *Journal of Fluid Mechanics*, Vol. 45, Pt. 3, Feb. 1971, pp. 477–512.

[9]Carling, J. C., and Hunt, B. L., "The Near Wall Jet of a Normally Impinging, Uniform, Axisymmetric, Supersonic," *Journal of Fluid Mechanics*, Vol. 66, Pt. 1, Oct. 1974, pp. 159–176.

[10]Lamont, P. J., and Hunt, B. L., "The Impingement of Underexpanded Axisymmetric Jets on Perpendicular and Inclined Flat Plates," *Journal of Fluid Mechanics*, Vol. 100, Pt. 3, Oct. 1980, pp. 471–511.

[11]Gubanova, O. I., Lunev, V. V., and Plastinina, L. N., "The Central Breakaway Zone with Interaction Between a Supersonic Underexpanded Jet and a Barrier," *Fluid Dynamics*, Vol. 6, July 1973, pp. 298–301.

[12]Ginzberg, I. P., Semilentenko, B. G., Terpigorev, V. S., and Uskov, V. N., "Some Singularities of Supersonic Underexpanded Jet Interaction with a Plane Obstacle," *Journal of Engineering Physics*, Vol. 19, 1973, pp. 1081–1084.

[13]Gummer, J. H., and Hunt, B. L., "The Impingement of a Non-Uniform, Axisymmetric, Supersonic Jet on a Perpendicular Flat Plate," *Israel Journal of Technology*, Vol. 12, No. 3–4, 1974, pp. 221–235.

[14]Alvi, F. S., and Iyer, K. G., "Mean and Unsteady Flowfield Properties of Supersonic Impinging Jets with Lift Plates," AIAA Paper 99-1829, May 1999.

[15]Wlezien, R. W., Bower. W. W., Childs, M. S., Howe, M. S., and Kibens, V., "Experimental and Computational Investigation of Supersonic STOVL Jet Flow and Acoustic Fields," NASA CR 189547, Jan. 1992.

[16]Ladd, J. A., and Korakianitis, T., "On the Assessment of One- and Two-Equation Turbulence Models for the Computation of Impinging Jet Flowfields," AIAA Paper 96-2545, July 1996.

[17]Wardwell, D. A., Hange, C., Kuhn, R. E., and Stewart, V. R., "Jet-Induced Ground Effects on a Parametric Flat-Plate Model in Hover," NASA TM 104001, 1993.

[18]Lourenco, L. M., and Krothapalli, A., "Mesh-Free Second Order Accurate Algorithm for PIV Processing," *Proceedings of the International Conference on Optical Technology and Image Processing in Fluid, Thermal and Combustion Flows*, Visualization Society of Japan, Yokohama, Japan, 1998, p. 224.

[19]Ross, C., Lourenco, L., and Krothapalli, A., "PIV Measurements in a Shock-Containing Supersonic Flow," AIAA Paper 94-0047, Jan. 1994.

[20]Bush, R. H., "A Three Dimensional Zonal Navier Stokes Code for Subsonic Through Hypersonic Propulsion Flowfields," AIAA Paper 88-2830, July 1988.

[21]Cain, A. B., and Bush, R. H., "Numerical Wave Propagation Analysis for Stretched Grids," AIAA Paper 94-0172, Jan. 1994.

[22]Spalart, P. R., and Allmaras, S. R., "A One-Equation Turbulence Model for Aerodynamic Flows," AIAA Paper 92-0439, Jan. 1992.

[23]Menter, F. R., "Zonal Two Equation $k-\omega$ Turbulence Models for Aerodynamic Flows," AIAA Paper 93-2906, July 1993.

[24]Spalart, R. R., and Shur, M. L., "On the Sensitization of Turbulence Models to Rotation and Curvature," *Aerospace Science and Technology*, Vol. 1, No. 5, 1997, pp. 297–302.

[25]Launder, B. E., Priddin, C. H., and Sharma, B. I., "The Calculation of Turbulent Boundary Layers on Spinning and Curved Surfaces," *Journal of Fluids Engineering*, Vol. 99, No. 1, 1977, pp. 231–239.

[26]Park, S. V., and Chung, M. K., "Curvature-Dependent Two-Equation Model for Prediction of Turbulent Recirculating Flows," *AIAA Journal*, Vol. 27, No. 3, 1989, pp. 340–344.

[27]Mani, M., Ladd, J. A., and Bower, W. W., "An Assessment of Rotation and Curvature Correction to One- and Two-Equation Turbulence Models for Compressible Impinging Jet Flows," AIAA Paper 2000-2406, June 2000.

[28]Wilcox, D. C., "Reassessment of the Scale Determining Equation for Advanced Turbulence Models," *AIAA Journal*, Vol. 26, No. 11, 1988, pp. 1299–1310.

[29]Jones, W. P., and Launder, B. E., "The Calculation of Low-Reynolds-Number Phenomena with a Two-Equation Model of Turbulence," *International Journal of Heat and Mass Transfer*, Vol. 16, No. 6, 1973, pp. 1119–1130.

[30]Bradshaw, P., "Compressible Turbulent Shear Layers," *Annual Review of Fluid Mechanics*, Vol. 9, 1977, pp. 33–54.

[31]Kalghatgi, G. T., and Hunt, B. L., "The Occurrence of Stagnation Bubbles in Supersonic Jet Impingement Flows," *Aeronautical Quarterly*, Vol. 27, Aug. 1976, pp. 169–185.

[32]Alvi, F. S., Elavarasan, R., Shih, C., Garg, G., and Krothapalli, A., "Active Control of Supersonic Impinging Jets Using Microjets," AIAA Paper 2000-2236, June 2000.

[33]Kitamura, S., and Iwamoto, J., "Numerical Analysis of Supersonic Impinging Jet," *Transactions of the Japan Society for Aeronautical and Space Sciences*, Vol. 41, No. 132, 1998, pp. 57–64.

[34]"JSF Surface Erosion Materials Characterization Program Test Results," R.G.A. Angel, British Aerospace PLC, FAE-R-RES-4620, Issue 1, April 1999.

[35]Messersmith, N. L., and Murthy, S. N. B., "Thermal and Mechanical Loading on a Fire Protection Shield Due to a Combustor Burn-Through," *Propulsion and Energetics Panel (PEP) 88th Symposium*, CP-587, AGARD, 1996, pp. 22-1–22-13.

M. Sichel
Associate Editor